

Received 25 May 2025, accepted 20 June 2025, date of publication 4 July 2025, date of current version 21 July 2025.

Digital Object Identifier 10.1109/ACCESS.2025.3586121

RESEARCH ARTICLE

AI and Digital Twin Federation-Based Flexible Safety Control for Human–Robot Collaborative Work Cell

JI DONG CHOI^{1,3}, SEUNG-HWAN CHOI^{2,3}, MIN YOUNG KIM¹, (Member, IEEE),
INHO LEE², (Member, IEEE), SUWOONG LEE³, AND BYEONG HAK KIM³

¹School of Electronic and Electrical Engineering, Kyungpook National University, Daegu 41566, Republic of Korea

²Department of Electronics Engineering, Pusan National University, Busan 46241, Republic of Korea

³Korea Institute of Industrial Technology, Daegu 41061, Republic of Korea

Corresponding authors: Suwoong Lee (lee@kitech.re.kr) and Byeong Hak Kim (bhkim81@kitech.re.kr)

This work was supported in part by the Industrial Technology Innovation Program, through the Development of a Near-Field Optimized Camera Image Fusion Ultra-High Resolution LiDAR System, under Grant RS-2024-00423589; and in part by the Ministry of Trade, Industry and Energy (MOTIE, South Korea), through the Robot and Robot Service Digital Twinization Framework Technology, under Grant RS-2024-00424974.

ABSTRACT This paper proposes a safety response technology that leverages multi-domain vision sensors to monitor the positions of workers and robots in real-time, enabling dynamic calculation of Flexible Protective Separation Distances (FPSD) for adaptive robot velocity control and safety stops. Compliant with ISO/TS 15066 technical specifications for speed and separation monitoring, the method integrates AI-driven 3D pose estimation and Digital Twin visualization to enhance safety and productivity in human-robot collaborative (HRC) work cells. Experimental results demonstrate that FPSD significantly outperforms static Protective Separation Distance (PSD) methods, achieving collaboration times of 2.50 s (98.04%) and 5.40 s (99.08%) in gantry and collaborative robot experiments, respectively, compared to 0.25 s (9.80%) and 2.50 s (45.87%) for PSD method. The system reduces unnecessary robot pauses with average response times of 0.021 s for deceleration and 0.032 s for stops, ensuring robust collision prevention. Validated using multi-domain sensor data in dynamic HRC tasks, this approach confirms its potential for scalable deployment in smart manufacturing, offering a flexible and efficient safety framework.

INDEX TERMS Digital twin, AI, robot work cell, protective separation distance (PSD), safety control.

I. INTRODUCTION

In recent years, the adoption of collaborative robots in manufacturing has grown significantly, driven by the demand for flexible work environments and improved productivity. These robots, designed to comply with ISO/TS 15066:2016 technical specifications [1], ensure safe human-robot collaboration (HRC). A critical feature, Power and Force Limiting, imposes strict constraints on biomechanical quantities, such as contact force or pressure, on humans, keeping them below injury thresholds [2]. However, many existing safety systems struggle to adapt to the dynamic movements of workers and robots in real time. Static safety measures, such as fixed

Protective Separation Distance (PSD) or predefined velocity limits, often result in overly cautious robot behavior, limiting workspace flexibility, and reducing operational efficiency. To address these challenges, this study proposes a flexible safety control technology that leverages real-time data to dynamically adjust safety parameters while adhering to ISO/TS 15066:2016, enhancing both safety and productivity in dynamic manufacturing settings.

Speed and Separation Monitoring (SSM), a critical mechanism in collaborative robotics, prevents physical contact by maintaining a Protective Separation Distance (PSD) between humans and robots, as outlined in ISO/TS 15066, ISO 10218-1, ISO 10218-2, and ISO 13855 [3], [4], [5]. Effective human-robot collaboration (HRC) requires real-time PSD adjustments to enable closer interaction without

The associate editor coordinating the review of this manuscript and approving it for publication was R. K. Tripathy¹.

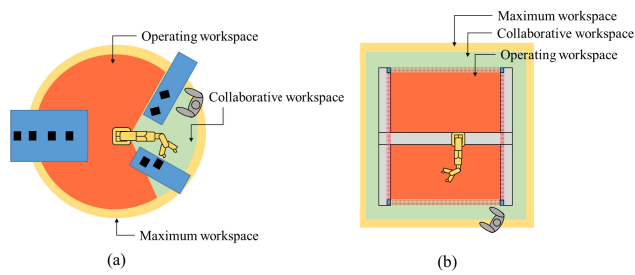


FIGURE 1. Examples of worker-robot collaborative workspaces. (a) Workspace for a worker and a collaborative robot, (b) Workspace for a worker, a collaborative robot, and a gantry robot.

compromising safety. Conventional SSM systems, as shown in Figure 1, typically rely on torque sensors for impact detection and laser curtain sensors for spatial awareness [6]. However, these solutions, designed for static PSDs, struggle in dynamic HRC environments with unpredictable worker movements or varying task demands, leading to frequent, unnecessary robot pauses that significantly reduce collaboration time (e.g., 9.80% and 54.94% for PSD method#1 and #2, respectively, as shown in Table 7). Our proposed Flexible Protective Separation Distance (FPSD) approach addresses these limitations by leveraging real-time multi-domain sensor data to track worker and robot movements, enabling adaptive PSD adjustments. Experimental results demonstrate that FPSD substantially enhances collaboration time (98.04% and 99.08% in Table 7) and ensures safer, more continuous workflows (Tables 5, 6). Direct comparison with existing SSM implementations is constrained due to differences in system design (static vs. adaptive PSD), sensor configurations, and task objectives (static safety vs. dynamic interaction), but our findings highlight FPSD's superior flexibility and productivity while maintaining compliance with ISO standards.

Industrial safety standards, including ISO 10218-1 and ISO 10218-2, provide general guidelines for collaborative robot operations, while ISO/TS 15066 offers detailed HRC safety requirements [7], [8], [9]. According to ISO 10218-2, robots in automatic mode must stop if a worker enters their working radius [10]. ISO/TS 15066 defines PSD as the minimum allowable distance between a robot and an operator, calculated using the minimum distance formula of ISO 13855 based on the speed of human approach [11]. Building on these standards,

This paper introduces three key contributions:

- 1) A multi-domain vision sensing system for precise 3D worker position tracking AI model.
- 2) An AI and Digital Twin federation technology to enable real-time safety control and workspace visualization in robot-worker collaborative environments by processing multidomain sensor and robot data at 10ms intervals.
- 3) A FPSD algorithm that optimizes workspace utilization while meeting safety standards.

The paper is organized as follows: Section II reviews related work, Section III details the proposed AI-based

Digital Twin safety technique, Section IV presents experimental results, and Section V concludes with future research directions.

II. RELATED WORK

Extensive research has explored the safety of collaborative robots from diverse perspectives, focusing on enhancing HRC in manufacturing environments. Villani et al. [12] proposed a suite of strategies and algorithms to bolster collaborative robot safety, leveraging technologies such as collision detection, force control, and path planning. Their work demonstrated significant improvements in robotic system safety, offering robust mechanisms to mitigate collision risks. However, it lacks real-time adaptability to dynamic worker movements and complex workspace configurations, limiting its applicability in highly variable HRC tasks where operational flexibility is critical. Similarly, Haddadin et al. [13] tackled safety challenges in physical human-robot interaction by establishing systematic safety control strategies and design principles, validated through practical use cases. Their approach excels in ensuring biomechanical safety during contact scenarios, but its dependence on static, sensor-based PSD often compromises operational efficiency, as it cannot dynamically adjust to fluctuating worker-robot interactions.

Standardized methodologies for assessing collaborative robot safety represent another key research area. Lasota et al. [14] developed benchmarks and quantitative metrics for evaluating safety, creating a data-driven safety assessment framework based on industrial site measurements. This enables objective comparisons of safety performance across systems, providing a scalable evaluation tool. Yet, their framework primarily focuses on static safety metrics, overlooking dynamic interactions that affect real-time HRC performance. Robla-Gómez et al. [15] introduced a virtual reality (VR)-based method to assess HRC safety, using simulations to preemptively identify risks across collaboration scenarios. While this approach excels in predictive risk analysis and scenario testing, its reliance on simulated environments may not fully capture the unpredictability of real-world HRC dynamics.

Recent advancements have increasingly incorporated artificial intelligence (AI) to enhance collaborative robot safety. Cheng et al. [16] proposed an automated method for learning safe control policies using deep reinforcement learning, validated in simulated robotic systems. This offers adaptive decision-making capabilities, improving robot responsiveness to environmental changes—a clear advantage over traditional rule-based systems. However, its computational complexity and simulation-based validation limit immediate deployment in real-time industrial settings. Liu et al. [17] developed a deep learning model for predicting human behavior, enabling real-time trajectory planning for safe robot operation. This predictive approach enhances proactive collision avoidance, but its accuracy depends heavily on training data quality, potentially faltering in diverse or untrained HRC scenarios.

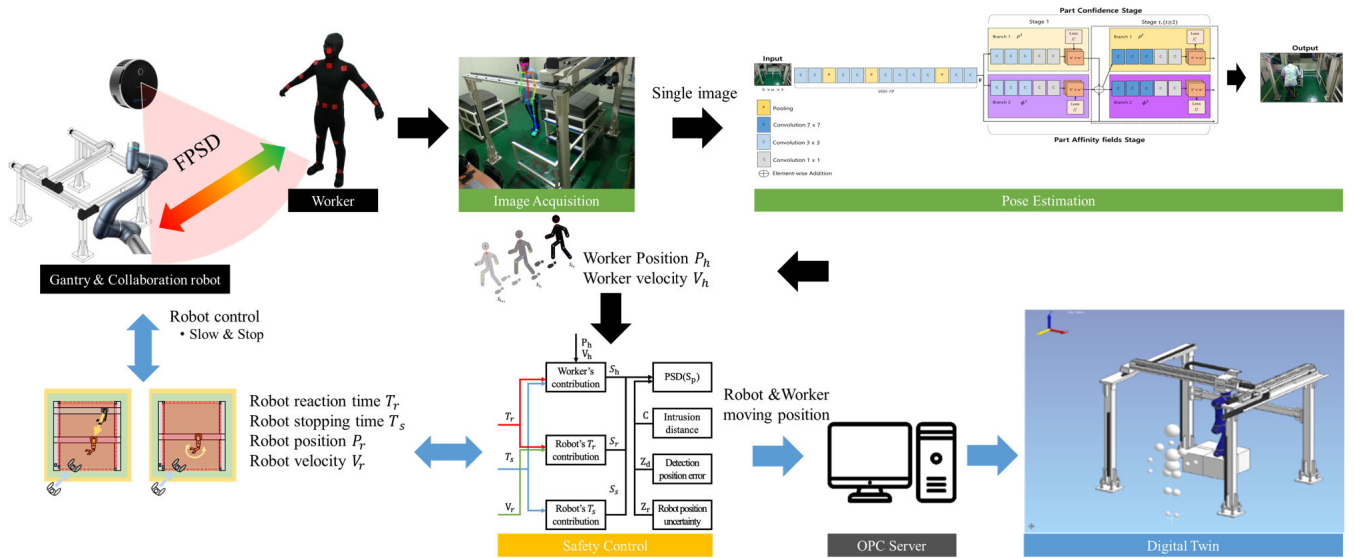


FIGURE 2. Proposed pipeline for AI and digital twin-based safety control in Human-Robot collaboration. The pipeline integrates multi-domain sensor data processing (upper branch) with real-time digital twin visualization (lower branch), synchronized at 10 ms intervals to ensure adaptive safety control and workspace monitoring.

Further efforts have focused on collision prevention and efficiency optimization in HRC environments, with PSD calculation emerging as a critical factor. Himmelsbach et al. [18] evaluated PSDs per ISO/TS 15066 standards, testing worker velocities of 0.25, 1.6, and 2.5 m/s and robot velocities from 0 to 2.5 m/s. Their work improved workspace efficiency by tailoring safety distances to specific velocity profiles, yet the fixed velocity assumptions fail to accommodate real-time variations in worker behavior. Karagiannis et al. [19] fixed worker velocity at 1.6 m/s per ISO/TS 15066, adjusting robot velocities (2, 0.25, and 0 m/s) across dynamic safety zones. This zoned approach enhances safety zoning flexibility, but its static worker velocity model restricts adaptability to spontaneous movements. Podgorelec et al. [20] explored PSDs with worker velocities of 0.25, 1.6, and 2.5 m/s and robot velocities of 0, 0.5, 1.0, and 2.0 m/s, comparing results with prior studies. Their comprehensive velocity range analysis provides valuable benchmarks, but the predetermined settings overlook real-time worker-robot interplay, reducing practical efficiency.

Collectively, these studies highlight key strengths in HRC safety, such as robust collision mitigation, scalable assessment tools, predictive AI capabilities, and optimized PSDs. However, their common limitations—namely, insufficient real-time adaptability, reliance on static parameters, and limited handling of dynamic interactions—underscore the need for a flexible, adaptive safety framework. This work addresses these gaps by integrating real-time multi-domain sensing and AI-driven PSD adjustments to balance safety and productivity in HRC tasks.

Recent advancements in large-area sensing and velocity adaptation have enhanced HRC safety systems. Yang et al. [21] developed a Digital Twin-based robot skin

system for healthcare robots, using multi-domain sensing for safe human-centered interaction, though focused on Healthcare 4.0 scenarios. Similarly, Gbouna et al. [22] proposed a scalable robot skin with sensor fusion for safer telehealthcare HRC, but it lacks real-time adaptability for dynamic industrial settings. Wang et al. [23] introduced a hierarchical proximity sensing framework for smooth velocity transitions in HRC, complementing our FPSD approach, though its computational complexity may limit real-time industrial use. Pang et al. [24] surveyed robot skin technologies, highlighting their role in safe collaboration and teleoperation, supporting our integration of real-time multi-domain sensing and adaptive FPSD to address static safety parameter limitations in dynamic HRC environments.

III. PROPOSED METHOD

This section outlines the proposed method for enhancing safety and productivity in HRC work cells through a flexible safety control system. The overall pipeline of this method, illustrated in Figure 2, integrates multi-domain sensing, AI-driven safety control, and Digital Twin visualization into a cohesive framework. The pipeline operates across two branches: the upper branch processes multi-domain sensor data and robot motor data at 10 ms intervals to estimate worker poses, compute FPSD, and execute real-time safety controls, while the lower branch uses the processed data to visualize the collaborative workspace via a Digital Twin. Data synchronization between the branches ensures consistent and real-time information sharing, enabling adaptive responses to dynamic worker-robot interactions. The following subsections elaborate on each component: multi-domain sensing for 3D worker pose estimation (Section III-A), AI and Digital Twin federation (Section III-B), FPSD calculation

(Section III-C), and the FPSD algorithm for safety control (Section III-D).

A. 2D AND 3D MULTI-DOMAIN SENSING FOR WORKER POSE ESTIMATION

In industrial manufacturing settings, interactions between stationary workpieces and dynamically operated collaborative robots, gantry robots, and human operators frequently induce occlusion phenomena, obstructing the detection of certain body parts of the operator. This occlusion effect poses significant challenges in accurately assessing the dynamic interactions and spatial constraints between robotic systems and moving operators. To address these limitations, the proposed system employs a multi-domain vision sensor framework, as part of the pipeline shown in Figure 2, to precisely estimate the operator's 3D skeletal position by integrating multidimensional sensor data, suppressing noise, and compensating for data loss caused by occlusion.

To robustly track operator motion within the collaborative workspace, 2D skeletal position data is extracted from dynamically moving operators using the OpenPose model [25]. For precise 3D skeletal position estimation, this 2D skeletal data is reprojected onto depth maps generated by the multi-domain vision sensor system, effectively embedding depth information into the 2D coordinates to derive 3D spatial positions. The 3D skeletal positions, independently computed from each sensor, are subsequently fused to produce a cohesive 3D skeletal dataset. This fusion process leverages the Iterative Closest Point (ICP) algorithm [26] to estimate rotation and translation matrices between 3D point cloud datasets acquired from multiple viewpoints, yielding spatially aligned 3D skeletal positions.

To unify the 3D skeletal positions estimated from multiple viewpoints into a single coordinate system, the frontal perspective is designated as the reference frame. The 3D skeletal data from the left viewpoint is processed using the ICP algorithm to derive rotation and translation matrices relative to the frontal reference. These matrices are then applied to the left-side 3D skeletal data to achieve spatially aligned 3D skeletal positions. The alignment accuracy is evaluated by calculating the Euclidean distance d between multi-view 3D skeletal datasets, as formulated in Equation (1):

$$d(R_i L_i) = \sqrt{(x_l - x_r)^2 + (y_l - y_r)^2 + (z_l - z_r)^2} \quad (1)$$

Here, x_l , y_l , z_l and x_r , y_r , z_r represent the 3D skeletal position coordinates obtained from distinct viewpoints (e.g., frontal and left), while R_i and L_i denote the i -th 3D skeletal position data of the dynamic operator at different time instances.

For temporally aligned 3D skeletal data, sorting is performed based on the Euclidean distance d , and data points with a distance below a threshold of 0.4 are matched and

aggregated, as described in Equation (2):

$$p_{reg} = \left\{ \frac{1}{n} \sum_{i=1}^n R_i \mid d(R_i L_i) < \text{thresh} \right\} \quad (2)$$

Here, p_{reg} is the averaged 3D skeletal position dataset from matched multi-viewpoint data; R_i is the i -th 3D skeletal point from the frontal viewpoint; L_i is the i -th 3D skeletal point from the left viewpoint; $d(R_i, L_i)$ is the Euclidean distance between R_i and L_i ; thresh is the 0.2 m threshold, where distances above are noise and below are matched; n is the count of matched points meeting the threshold.

The adoption of a minimal configuration of two sensors (e.g., an RGB camera and a depth sensor) within the multi-domain vision sensor system is justified by several engineering considerations. First, efficiency and computational resource optimization are critical; increasing the number of sensors escalates data throughput and computational complexity, potentially compromising real-time system performance. A dual-sensor setup effectively addresses occlusion while maintaining computational efficiency. Second, spatial coverage and data complementarity are ensured by strategically positioning the two sensors to capture multiple perspectives (e.g., frontal and lateral), compensating for blind spots and enhancing the 3D reconstruction process. Third, real-time performance assurance is paramount, with a requirement to process data at 10-ms intervals for safety-critical applications (refer to Table 1). Minimizing sensor count reduces fusion and communication latency, satisfying these stringent timing constraints.

In addition to these technical justifications, practical constraints of the manufacturing environment were also considered. As shown in Figure 4, the operational space of the robot workcell is limited to approximately $3\text{m} \times 3\text{m} \times 2\text{m}$, and excessive sensor installations would unnecessarily expand the physical footprint of the safety system, disrupting efficient workspace layout. Given the field of view and sensing range of the Intel RealSense L515 sensor, deploying two strategically placed units was found to be sufficient to fully cover the target area while minimizing occlusion. Therefore, from both system performance and spatial design perspectives, a dual-sensor configuration represents the optimal trade-off between accuracy, coverage, and operational feasibility for this specific application scenario.

B. FEDERATION OF AI AND DIGITAL TWIN

Digital Twin-based human-robot collaboration technology facilitates efficient monitoring and optimization of work processes in smart manufacturing environments by replicating the physical environment as a three-dimensional digital model [27], [28]. This concept relies on seamless integration between physical and virtual systems, where the Digital Twin is defined as a digital representation that reflects real-world entities such as machines, processes, and workers in real time, enabling dynamic adaptation through bidirectional data exchange [29], [30], [31].

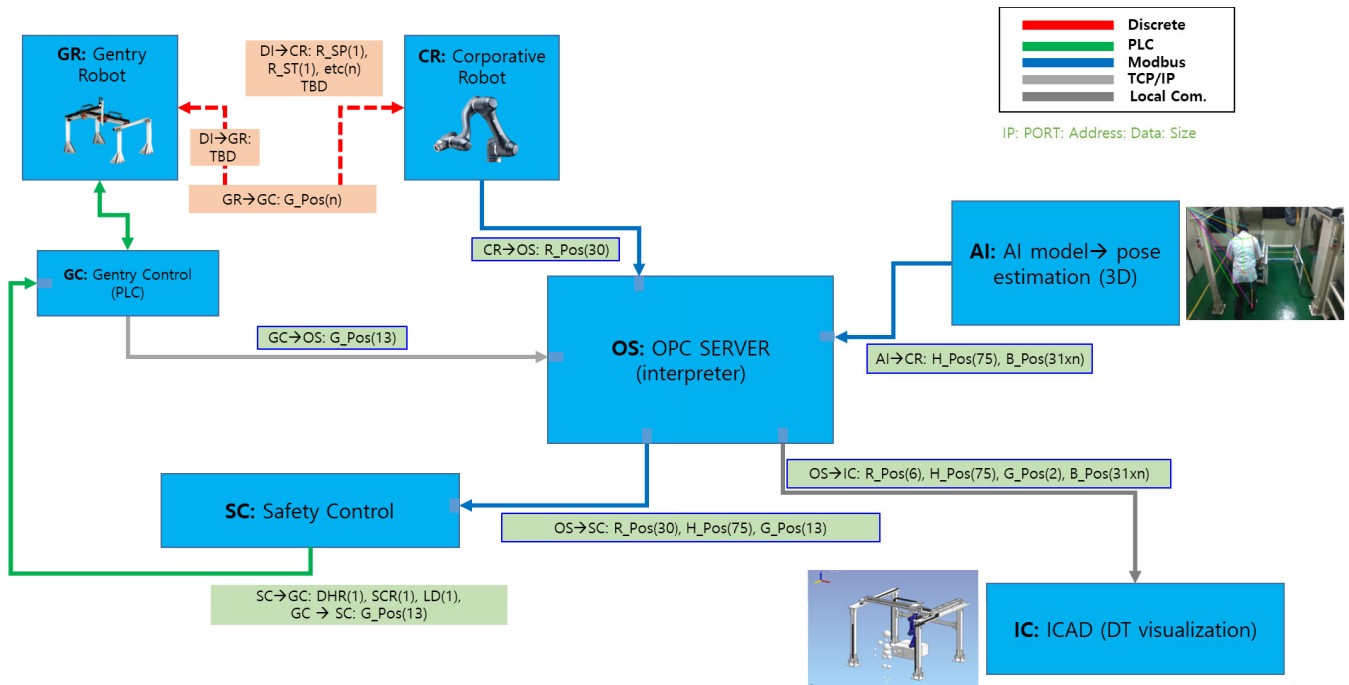


FIGURE 3. System integration and data interface design for AI and digital twin federation. The diagram illustrates the data flow from the AI-driven perception and control module (upper branch) to the digital twin visualization module (lower branch), synchronized at 10 ms intervals for real-time safety control in collaborative work cells.

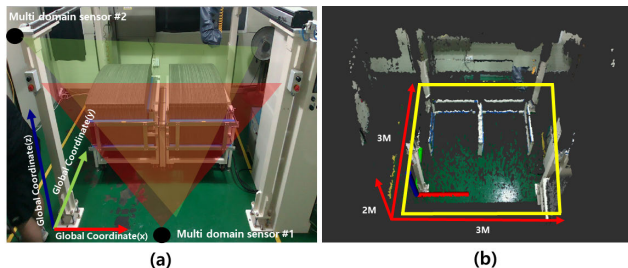


FIGURE 4. Multi-domain sensor placement strategy for Human-Robot collaborative work cells. (a) Optimal placement of two Intel RealSense L515 sensors to maximize field-of-view coverage and minimize occlusion for accurate 3D worker pose estimation. (b) Spatial layout of the 3m x 3m x 2m robot workcell.

With advancements in Industry 4.0, the integration of AI and Digital Twin serves as a core component of advanced safety control systems in human-robot collaborative work cells, as reflected in the system pipeline depicted in Figure 3 and the communication framework outlined in Table 1. The system comprises an AI-based perception and control module (upper branch) and a Digital Twin-based visualization module (lower branch), synchronized with a precise 10ms cycle to maximize operational safety and productivity.

In this architecture, the AI module acts as the reference clock, orchestrating all events—including sensor data acquisition, robot data communication, FPSD calculation, and data transmission to the Digital Twin—at fixed 10ms intervals. This cycle is ensured through a real-time operating system (RTOS) with hardware timers and an interrupt-driven event

loop, where each data packet includes a timestamp based on the fixed cycle for synchronization in downstream modules (e.g., PLC, ICAD). This mechanism maintains temporal consistency and reproducibility in data processing.

Table 1 summarizes the communication protocols and data formats used for real-time data exchange between the AI module, collaborative robots (CR), gantry robots (GR), and the Digital Twin visualization system, ensuring synchronized operation at 10 ms intervals for adaptive safety control in human-robot collaborative work cells. The AI module processes multi-domain sensor data at 10ms intervals to estimate the 3D joint positions and velocities of the human worker, adhering to the format defined in Table 1, Group 1 (H_Pos(75), H_Vel(n), Float16, units: mm, mm/s). Simultaneously, it collects position (R_Pos(75), G_Pos(15)), velocity (R_Vel(30), G_Vel(15)), and torque (R_Torq(30)) data from CR and GR via Modbus and PLC protocols, all synchronized to the 10ms cycle of the AI module's reference timer. Based on this data, the AI calculates the FPSD and executes adaptive safety control commands, such as deceleration or stopping of robots, depending on the relative position and velocity between the human and robots.

Within this framework, the AI module processes multi-domain sensor data at a 10ms interval to estimate the 3D skeletal positions and velocities of workers, as specified in Table 1, Group 1 (e.g., H_Pos(75) and H_Vel(n), Format: Float16, Units: mm and mm/s). Simultaneously, it interfaces with Modbus and PLC communication protocols to acquire motor data from CR and GR at the same 10ms cycle. This includes real-time position (R_Pos(75), G_Pos(15), velocity

TABLE 1. Communication and Data Description for CR and GR Robots. (OS: OPC Server, CR: Cooperative Robot, AI: AI model, GC: Gantry Control, IC: ICAD, SC: Safety Control.)

Num	Local	Dest	Communication	Data Description	Format	Unit
Group 1: Human Pose and Voxel Box Data						
1	OS	CR	Modbus	H_Pos(75) Dec: 500–575	Float16	mm
	AI	CR	Modbus	B_Pos(n) Dec: 600–605	Float16	mm
	AI	CR	Modbus	B_Pos(n) Dec: 606–629	Float16	mm
	AI	CR	Modbus	B_Pos(n) Dec: 630–698	Float16	mm
Group 2: CR Robot Axis 6 Angles						
2	CR	OS	Modbus	H_Pos(75) Dec: 500–575	Float16	mm
3	CR	OS	Modbus	R_Pos(30) Dec: 270–275	Int16	DEG
	CR	OS	Modbus	R_Pos(30) Dec: 280–285	Int16	DEG/SEC
	CR	OS	Modbus	R_Pos(30) Dec: 290–295	Int16	mA
	CR	OS	Modbus	R_Pos(30) Dec: 310–315	Int16	N/m
	CR	OS	Modbus	R_Pos(30) Dec: 400–402	Int16	mm
	CR	OS	Modbus	R_Pos(30) Dec: 403–405	Int16	DEG
Group 3: GR Robot Position and Control						
4	GC	OS	PLC	G_Pos(13) K80, K90	–	ON/OFF
	GC	OS	PLC	G_Pos(13) D1004-D, D1024-D	Int32	mm
	GC	OS	PLC	G_Pos(13) D1006, D1026	Int32	mm/sec
	GC	OS	PLC	G_Pos(13) P33–P35	–	ON/OFF
	GC	OS	PLC	G_Pos(13) K81, K82, K91, K92	–	ON/OFF
Group 4: CR Robot Axis 6 Angles (Local/OPC DA)						
5	OS	IC	Local/OPC DA	R_Pos(6) Dec: 270–275	Int16	DEG
	OS	IC	Local/OPC DA	H_Pos(75) Dec: 500–575	Float16	mm
	OS	IC	Local/OPC DA	G_Pos(24) D1004-D, D1024-D	Int32	mm
	OS	IC	Local/OPC DA	B_Pos(n) Dec: 600–605	Float16	mm
	OS	IC	Local/OPC DA	B_Pos(n) Dec: 606–629	Float16	mm
	OS	IC	Local/OPC DA	B_Pos(n) Dec: 630–698	Float16	mm
Group 6: Additional Robot Data (PLC)						
6	OS	SC	Modbus	R_Pos(30) Dec: 270–275	Int16	DEG
	OS	SC	Modbus	R_Pos(30) Dec: 280–285	Int16	DEG/SEC
	OS	SC	Modbus	R_Pos(30) Dec: 290–295	Int16	mA
	OS	SC	Modbus	R_Pos(30) Dec: 310–315	Int16	N/m
	OS	SC	Modbus	R_Pos(30) Dec: 400–402	Int16	mm
	OS	SC	Modbus	R_Pos(30) Dec: 403–405	Int16	DEG
	OS	SC	Modbus	H_Pos(75) Dec: 500–575	Float16	mm
	OS	SC	PLC	G_Pos(13) K80, K90	–	ON/OFF
	OS	SC	PLC	G_Pos(13) D1004-D, D1024-D	Int32	mm
	OS	SC	PLC	G_Pos(13) D1006, D1026	Int32	mm/sec
	OS	SC	PLC	G_Pos(13) P33–P35	–	ON/OFF
	OS	SC	PLC	G_Pos(13) K81, K82, K91, K92	–	ON/OFF
	OS	SC	Modbus	B_Pos(n) Dec: 600–605	Float16	mm
	OS	SC	Modbus	B_Pos(n) Dec: 606–629	Float16	mm
	OS	SC	Modbus	B_Pos(n) Dec: 630–698	Float16	mm
Group 5: Additional Robot Data						
7	SC	GC	PLC	DHR(1) K100	Float16	mm
	SC	GC	PLC	SCR(1) K101	Float16	mm/sec
	SC	GC	PLC	LD(1) K102	Int8	Level
	GC	SC	PLC	G_Pos(13) K80, K90	–	ON/OFF
	GC	SC	PLC	G_Pos(13) D1004-D, D1024-D	Int32	mm
	GC	SC	PLC	G_Pos(13) D1006, D1026	Int32	mm/sec
	GC	SC	PLC	G_Pos(13) P33–P35	–	ON/OFF
	GC	SC	PLC	G_Pos(13) K81, K82, K91, K92	–	ON/OFF

R_Vel(30), G_Vel(15)), and torque (R_Torq(30)), as detailed in Groups 2 and 3 of Table 1, with all data synchronized at 10ms intervals. Leveraging these data streams, the AI dynamically computes the FPSD, enabling adaptive safety responses—such as velocity reduction or emergency stops—based on the real-time relative positions and velocities of workers and robots.

The Digital Twin module, implemented using the ICAD tool, receives processed data from the AI module and robot systems at 10ms intervals (Table 1, Group 4: R_Pos(6), G_Pos(30), H_Pos(75)). This data is queued based on timestamps. The Digital Twin solely performs visualization, without involvement in control logic, reflecting the AI module's computed results to provide real-time 3D visualization of human-robot interactions.

Communication with robots via Modbus and PLC protocols is managed with a retry mechanism that attempts retransmission up to three times in case of a timeout (5ms

threshold). Upon repeated failures, the system activates an error flag, immediately halting robot operations and pausing the Digital Twin visualization to prevent discrepancies or safety incidents between the physical and virtual systems.

The overall pipeline, as shown in Figure 3, consists of two interconnected branches: the upper branch, where the AI performs real-time data processing and safety control, and the lower branch, where the Digital Twin visualizes the interactions in 3D. These branches are precisely coordinated through a reference clock-based real-time data synchronization structure, clearly separating control and visualization to ensure system safety and reproducibility.

This architecture was validated through experimental scenarios involving workers and robots operating at varying speeds. Compared to conventional systems using fixed PSD, the proposed system achieves greater flexibility and productivity by dynamically adjusting the FPSD at a 10ms resolution. The synchronized integration of AI's computational

Algorithm 1 Integrated Safety System for Human-Robot Collaboration

Require: $PC_1, PC_2, R = (pos_r, vel_r), \delta = 0.2, T_r = 0.111s, T_s = 0.312s, S_s = 0.2574m, R_c = 0.9m, J_s = 0.286rad, \alpha = 1.5, \Delta t$

Ensure: Safety level $\in \{0, 1, 2\}$

```

1 Pose Estimation Fusion
1: tree  $\leftarrow$  CreateKDTree( $PC_2$ ) {Build KD-tree for  $PC_2$ }
2: distances, indices  $\leftarrow$  tree.Query( $PC_1$ ) {Query nearest neighbors}
3:  $H_{pos} \leftarrow \emptyset$ 
4: matched  $\leftarrow \emptyset$ 
5: for  $i \in \{1, \dots, |PC_1|\}$  do
6:   if distances[ $i$ ]  $< \delta$  then
7:      $H_{pos}.append(PC_2[indices[i]])$  {Add matched point from  $PC_2$ }
8:     matched.add(indices[ $i$ ])
9:      $H_{pos}.append(PC_1[i])$  {Add corresponding point from  $PC_1$ }
10:  end if
11: end for
12: unmatched  $\leftarrow \{1, \dots, |PC_2|\} \setminus matched$  {Identify unmatched points}
13:  $H_{pos}.extend(PC_2[unmatched])$  {Add unmatched points to  $H_{pos}$ }
2 Velocity Estimation
14:  $\vec{v}_h \leftarrow$  EstimateVelocity( $H_{pos}, prev\_H_{pos}, \Delta t$ ) {Estimate human velocity}
3 Safety Control
15: FPSD  $\leftarrow |\vec{v}_h|(T_r + T_s) + |\vec{v}_r|T_r + S_s$  {Compute safety distance}
16: dist  $\leftarrow \min\{|p - pos_r| : p \in H_{pos}\}$  {Find minimum distance to robot}
17: if dist  $<$  FPSD then
18:   Safety level: 2 (Emergency-stop) {Trigger emergency stop}
19: else if dist  $< \alpha \times FPSD$  then
20:   Safety level: 1 (Speed-slow) {Reduce speed}
21: else
22:   Safety level: 0 (Normal) {Operate normally}
23: end if

```

accuracy and the Digital Twin's visual clarity satisfies safety, efficiency, and reproducibility simultaneously in complex work environments.

C. FLEXIBLE PROTECTIVE SEPARATION DISTANCE

The direction and velocity of movement of the worker and robots are variable, and it is difficult to predict the relative velocity when the worker approaches the robot's workspace. Additionally, the robot must reduce its velocity or stop when the worker approaches the workspace to prevent collisions. The moment at which the robot should stop, based on the relative distance between the worker and the robot, varies depending on the robot's velocity, reaction time, stopping

distance, and the worker's approach velocity. This moment is defined in ISO/TS 15066 as the PSD, which is the minimum allowable distance between the robot and the person. The calculation formula for PSD (S_p) is as follows.

$$S_p(t_0) = S_h + S_r + S_s + C + Z_d + Z_r \quad (3)$$

Here, t_0 represents the current time, S_h denotes the contribution of the worker's position change to the distance, S_r represents the contribution of the robot system's reaction time, S_s signifies the contribution of the stopping distance of the robot system, C is the distance by which the worker encroaches into the workspace before any part of their body is detected, Z_d indicates the measurement error of the worker's position from the surveillance system, and Z_r represents the positional uncertainty of the robot system. The constant values of S_h , S_r , and S_s , which are the distances determined by the movement of the worker and the robot system, can be calculated using Equations (4), (5), and (6).

$$S_h = \int_{t_0}^{t_0+T_r+T_s} v_h(t)dt = v_h(t_0) \times (T_r + T_s) \quad (4)$$

$$S_r = \int_{t_0}^{t_0+T_r} v_r(t)dt = v_r(t_0) \times (T_r) \quad (5)$$

$$S_s = \int_{t_0+T_r}^{t_0+T_r+T_s} v_s(t)dt \quad (6)$$

Here, v_h represents the velocity at which the worker moves towards the robot's direction, v_r is the velocity of the robot moving towards the worker's direction within the workspace, v_s is the velocity that the robot has during the process of stopping, T_r is the time it takes for the robot to respond when a stop command is issued, and T_s is the time it takes for the robot to stop.

To safely control the robot in the workspace without collision accidents, an accurate PSD must be computed. In this paper, a more FPSD was calculated by applying the actual positions and speeds of the worker and robot, as shown in the block diagram in Figure 5.

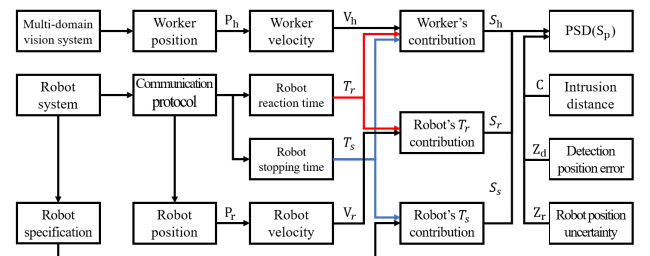


FIGURE 5. Block diagram for FPSD calculation.

To compute PSD (S_p), the worker's position and velocity were estimated using the multi-domain vision system proposed in Section III-B, and S_h was calculated. Additionally, the robot system utilized communication protocols such as Modbus and PLC to collect position and velocity data,

and calculate reaction time and stopping time to derive S_r and S_s . In this study, C was assumed to be zero because the surveillance system is capable of fully detecting the entire workspace. Z_d was calculated to be approximately 11.25 mm, based on the results in Table 2. Z_r is very small, as the robot's position information is directly received from the robot system. Specifically, according to the robot specifications, Z_r is approximately 0.0048 mm for the gantry robot and about 0.03 mm for the collaborative robot, which are negligible compared to the overall distance. Therefore, in this study, the values to C , Z_d , and Z_r were all set to zero in Equation (3) [18].

D. FLEXIBLE PROTECTIVE SEPARATION DISTANCE ALGORITHM FOR HUMAN-ROBOT COLLABORATION

This subsection presents an integrated safety control algorithm for HRC, leveraging worker pose estimation from multi-domain cameras and a FPSD. Detailed in Algorithm 1, this approach enhances workplace safety by detecting the worker's three-dimensional 3D position in real-time and dynamically computing separation distances from both gantry and collaborative robot systems, enabling adaptive safety responses.

The proposed algorithm, as outlined in Algorithm 1, consists of three main stages. In the first stage, point cloud data acquired from multi-domain cameras is fused to achieve robust 3D pose estimation. A KD-tree-based nearest neighbor search algorithm is employed to identify corresponding points between point clouds captured from different camera viewpoints. The matching is determined based on a distance threshold of $\delta = 0.2$. This threshold is a fixed value, empirically set to account for registration errors and sensor noise that may occur during fusion, and is designed to ensure stable 3D pose alignment regardless of environmental variations. Point pairs with spatial discrepancies exceeding 0.2 m are considered unreliable and thus excluded from the registration process. In this study, data from the second camera is prioritized for matched points due to its higher signal fidelity, while unmatched points retain their original values. This fusion strategy, built upon the multi-domain sensing framework presented in Section III-A, enables precise 3D skeletal alignment even under frequent occlusion conditions common in industrial environments.

In the second phase, the algorithm estimates the worker's velocity by analyzing positional changes across consecutive time frames, with a sampling interval (Δt) of 10 ms. Velocity vectors (\vec{v}_h) are derived to quantify dynamic worker movement, providing essential input for predictive safety distance calculations. This step enhances the system's responsiveness to real-time variations in worker behavior, a critical factor in HRC environments.

The third phase implements safety control by calculating FPSD, defined as the sum of three components: the worker's expected movement distance ($\|\vec{v}_h\|(T_r + T_s)$), the robot's expected movement distance ($\|\vec{v}_r\|T_r$), and a static safety distance ($S_s = 0.2574$ m). Here, T_r and T_s represent

the robot's reaction and stopping times (e.g., 0.111 s and 0.312 s for the collaborative robot, per Table 3), while S_s is determined based on the collaborative robot's maximum reach ($R_c = 0.9$ m) and the first joint's stopping distance ($J_s = 0.286$ rad). The system continuously compares the minimum distance between the worker and robot against FPSD, classifying the safety state into three levels: normal (level 0), speed-slow (level 1), or emergency-stop (level 2), as detailed in Algorithm 1. These levels are dynamically adjusted at 10 ms intervals to ensure real-time adaptability.

Unlike conventional systems reliant on static safety distances, this algorithm distinguishes itself by integrating real-time multi-domain data and phased safety controls. By accounting for the dynamic movements of both the worker and robot system, it achieves a predictive safety framework that balances stringent safety requirements (e.g., ISO/TS 15066) with operational efficiency. The practical implementation and experimental validation of this algorithm are demonstrated in Section IV-B, highlighting its ability to enhance productivity in HRC tasks while mitigating collision risks.

IV. EXPERIMENTS RESULTS

A. 2D AND 3D MULTI-DOMAIN SENSING FOR WORKER POSE ESTIMATION

The experimental setup in this study comprises four interconnected systems, integrated via PLC and Modbus communication protocols, each performing distinct functions. The multi-domain camera system, utilizing the Intel RealSense L515, is equipped with an Intel i7-12700H processor, an NVIDIA RTX 3070 Ti GPU, and 32GB RAM, enabling precise computation of the worker's 3D skeletal positions using RGB and thermal imaging data. The safety control system, powered by an Intel i7-13500H processor, Iris Xe Graphics GPU, and 32GB RAM, simultaneously governs the operations of the Doosan Robot (A-SERIES) and the Asys Technology Gantry Loader within the collaborative workspace. ICAD serves as the Digital Twin tool, providing real-time visualization of the 3D positions of the collaborative robot, the gantry robot, and the worker. Leveraging this hardware configuration, the 3D joint positions of the worker are estimated using the DeepMoCap framework [33]. In this experiment, a single subject executed and recorded six distinct motion scenarios, as depicted in Figure 6.

To elucidate the motion scenarios evaluated in Table 2, the following movements were defined: #1 represents a stationary upright posture (attention stance), #2 denotes a static pose with both arms extended laterally, #3 corresponds to a walking motion, #4 indicates a static posture holding a heavy load, #5 involves a dynamic pose with both arms widely spread horizontally, and #6 reflects a stationary stance following a large-step walking motion. These scenarios were selected to replicate typical worker behaviors in human-robot collaborative environments, encompassing both static and dynamic interactions.

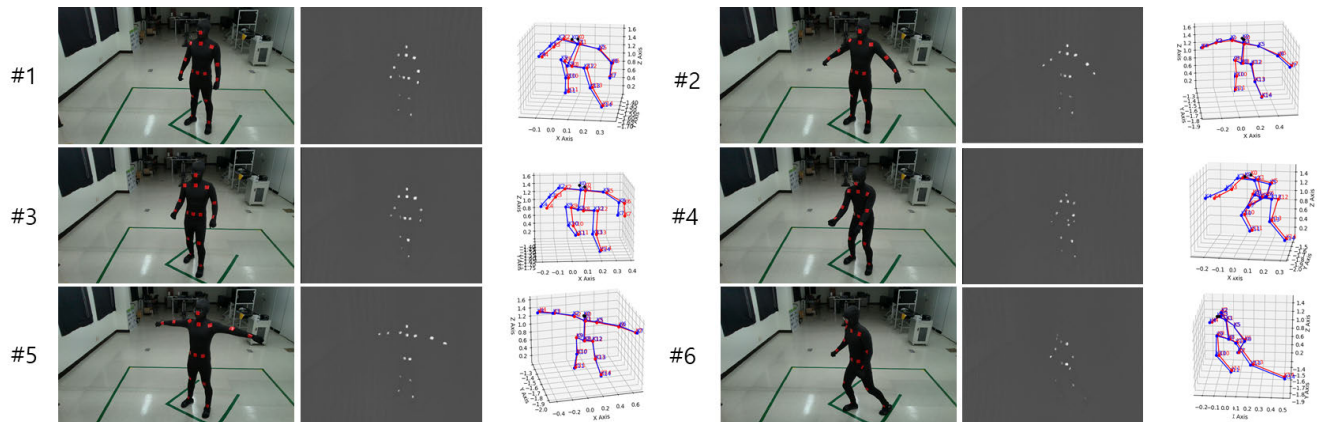


FIGURE 6. Comparison of 3D skeletal position estimation between RGB data and thermal imaging data for each action scenarios(#1 to #6).

TABLE 2. Comparison of 3D Skeletal Position Estimation Errors (cm) for Motion Scenarios #1 to #6 (3 Seconds, 30 FPS, 90 Frames).

ID(Body Parts)	Metric	#1	#2	#3	#4	#5	#6
0 (Head)	RMSE	1.33 ± 0.13	1.44 ± 0.14	1.69 ± 0.19	1.45 ± 0.20	1.12 ± 0.11	1.38 ± 0.13
	Min/Max	0.97/1.67	1.03/1.78	1.18/2.08	1.02/1.88	0.82/1.42	0.98/1.73
1 (Neck)	RMSE	0.94 ± 0.09	1.25 ± 0.12	1.29 ± 0.16	0.86 ± 0.10	0.55 ± 0.06	0.82 ± 0.08
	Min/Max	0.68/1.18	0.88/1.58	0.87/1.57	0.62/1.12	0.37/0.77	0.58/1.03
2 (Left Arm)	RMSE	0.87 ± 0.10	1.24 ± 0.13	0.95 ± 0.11	1.13 ± 0.14	1.27 ± 0.14	0.33 ± 0.06
	Min/Max	0.62/1.12	0.88/1.52	0.68/1.22	0.82/1.43	0.92/1.57	0.22/0.48
3 (Left Elbow)	RMSE	0.89 ± 0.09	0.47 ± 0.05	0.70 ± 0.10	1.37 ± 0.15	0.68 ± 0.09	0.44 ± 0.05
	Min/Max	0.67/1.07	0.33/0.63	0.52/0.92	0.98/1.67	0.47/0.87	0.28/0.58
4 (Left Hand)	RMSE	0.85 ± 0.11	0.73 ± 0.08	1.30 ± 0.17	2.40 ± 0.24	1.18 ± 0.15	1.04 ± 0.11
	Min/Max	0.62/1.07	0.48/0.93	0.88/1.62	1.78/2.87	0.82/1.47	0.73/1.32
5 (Right Arm)	RMSE	1.83 ± 0.15	0.76 ± 0.07	1.23 ± 0.12	1.33 ± 0.13	0.73 ± 0.06	0.76 ± 0.07
	Min/Max	1.32/2.23	0.53/0.98	0.88/1.52	0.97/1.63	0.52/0.92	0.53/0.98
6 (Right Elbow)	RMSE	1.22 ± 0.13	0.55 ± 0.06	0.36 ± 0.04	1.38 ± 0.14	1.06 ± 0.11	0.74 ± 0.08
	Min/Max	0.88/1.52	0.38/0.73	0.27/0.47	0.97/1.68	0.78/1.32	0.52/0.92
7 (Right Hand)	RMSE	1.48 ± 0.14	0.80 ± 0.08	1.12 ± 0.11	1.85 ± 0.18	1.61 ± 0.16	0.65 ± 0.07
	Min/Max	1.07/1.83	0.58/1.03	0.78/1.42	1.32/2.23	1.18/1.97	0.47/0.82
8 (Spine)	RMSE	0.73 ± 0.07	0.16 ± 0.04	0.51 ± 0.07	0.62 ± 0.07	0.49 ± 0.06	0.73 ± 0.09
	Min/Max	0.52/0.92	0.12/0.23	0.37/0.67	0.43/0.82	0.33/0.62	0.52/0.92
9 (Left Up Leg)	RMSE	0.93 ± 0.11	0.89 ± 0.10	0.72 ± 0.09	2.15 ± 0.23	0.87 ± 0.10	0.34 ± 0.04
	Min/Max	0.67/1.17	0.63/1.12	0.52/0.92	1.53/2.63	0.62/1.12	0.22/0.47
10 (Left Leg)	RMSE	0.50 ± 0.06	1.13 ± 0.14	0.75 ± 0.09	1.57 ± 0.18	0.89 ± 0.11	1.03 ± 0.11
	Min/Max	0.37/0.67	0.82/1.38	0.53/0.97	1.13/1.93	0.62/1.13	0.73/1.27
11 (Left Foot)	RMSE	2.13 ± 0.23	1.75 ± 0.19	1.60 ± 0.19	1.78 ± 0.20	1.26 ± 0.14	1.77 ± 0.19
	Min/Max	1.53/2.63	1.23/2.13	1.13/1.97	1.28/2.18	0.88/1.57	1.23/2.13
12 (Right Up Leg)	RMSE	0.34 ± 0.04	0.23 ± 0.03	0.68 ± 0.08	0.62 ± 0.07	0.94 ± 0.10	0.85 ± 0.09
	Min/Max	0.22/0.47	0.17/0.33	0.47/0.87	0.43/0.82	0.67/1.17	0.62/1.07
13 (Right Leg)	RMSE	0.63 ± 0.07	1.20 ± 0.13	0.93 ± 0.10	0.68 ± 0.08	0.88 ± 0.09	0.79 ± 0.08
	Min/Max	0.47/0.82	0.88/1.47	0.67/1.17	0.47/0.87	0.62/1.12	0.57/1.02
14 (Right Foot)	RMSE	1.74 ± 0.18	1.64 ± 0.17	1.97 ± 0.20	1.70 ± 0.19	1.40 ± 0.15	1.94 ± 0.19
	Min/Max	1.23/2.13	1.17/1.97	1.37/2.47	1.23/2.03	0.97/1.72	1.37/2.33
mAP RGB		1.17 ± 0.11	0.99 ± 0.09	1.09 ± 0.10	1.58 ± 0.15	1.00 ± 0.09	0.92 ± 0.08
		0.92/1.58	0.90/1.09	0.99/1.19	1.43/1.73	0.91/1.10	0.83/1.01
mAP Thermal		1.02 ± 0.09	0.87 ± 0.07	0.95 ± 0.09	1.42 ± 0.13	0.86 ± 0.07	0.78 ± 0.06
		0.87/1.17	0.78/0.96	0.86/1.04	1.28/1.56	0.77/0.95	0.70/0.86

For quantitative analysis, the Root Mean Square Error (RMSE) for 3D position estimation of each body part was calculated according to Equation (7). Table 2 presents the

positional errors in the x, y, and z coordinates of each body part, derived from RGB and thermal imaging data, validating the efficacy of the proposed multi-domain sensor approach.

Higher errors were observed in the hands, feet, and neck regions due to occlusion effects, while other body parts exhibited relatively low errors. The mean Average Precision (mAP), defined as the average precision across all body parts for each motion scenario (#1 to #6), quantifies the overall accuracy of 3D pose estimation, with results reported at the bottom of Table 2.

Single-domain vision systems face limitations due to occlusion, but the proposed multi-domain sensor system demonstrates enhanced robustness by analyzing data over 3 seconds at 30 FPS (totaling 90 frames). Table 2 includes RMSE, standard deviation, minimum/maximum errors, and mAP for RGB and thermal data, confirming error stability across the 90 frames. These improvements reinforce the real-time 3D position estimation accuracy of the multi-domain sensor system and the reliability of the safety control framework compliant with ISO/TS 15066 standards.

$$RMSE = \sqrt{\frac{\sum_{i=1}^n (x_{r,i} - x_{t,i})^2}{n}} \quad (7)$$

Here, $x_{r,i}$ represents the RGB data value in frame i , $x_{t,i}$ represents the thermal image data value in frame i , and n represents the total number of frames evaluated.

B. FPSD BASED SAFETY CONTROL

In this paper, the gantry robot and the collaborative robot were operated independently rather than simultaneously, in compliance with the regulations specified in ISO 10218-2. The experimentally measured average velocities, reaction times (T_r), and stopping times (T_s) of the gantry robot and the collaborative robot are summarized in Table 3. The FPSD was calculated based on the specifications of the faster-moving collaborative robot, taking into account the characteristics of the robot system.

TABLE 3. Parameters of specifications measured from the robots.

Robot Type	Velocity	T_r	T_s
Gantry Robot	80 mm/s	0.01 s	0.06 s
Collaborative Robot	450 mm/s	0.11 s	0.31 s

In this study, the FPSD was calculated by reflecting the real-time velocities of both the worker and the robot, and the proximity distance between them was used to implement safe robot velocity control. To this end, the system compared the real-time FPSD with the actual proximity distance to determine the risk, and the response time (T_{re}) required to transmit a deceleration or stop command to the robot was used as a performance metric. The experiment was conducted under the assumption that a worker approaches a robot in operation, and T_{re} was measured as the time it took for the system to detect the risk and transmit the control command to the robot. Table 4 presents the measured T_{re} results when

the worker approached within the FPSD-slow and FPSD-stop distances.

TABLE 4. Safety control response time of the robot based on FPSD.

No	FPSD slow (m)	T_{re} (s)	FPSD stop (m)	T_{re} (s)
1	1.299	0.017	0.978	0.016
2	1.306	0.025	0.934	0.051
3	1.345	0.015	0.930	0.042
4	1.356	0.015	0.945	0.023
5	1.336	0.021	0.954	0.036
6	1.312	0.016	0.937	0.032
7	1.309	0.027	0.953	0.029
8	1.308	0.015	0.950	0.025
9	1.307	0.027	0.909	0.045
10	1.278	0.027	0.912	0.016
Avg	1.316	0.021	0.940	0.032

As a result of conducting 10 experiments each for FPSD-slow and FPSD-stop, the average response times were 0.021 s and 0.032 s, respectively. These results confirm that the system can detect risk and transmit a deceleration or stop command within approximately 0.03 s, allowing the robot to respond safely and effectively. Although all safety stops were successfully triggered according to the FPSD-based control logic, it should be noted that false positive and false negative rates were not separately evaluated. This is because all stop events in the experiment were deliberately induced and verified under controlled conditions, and thus can be regarded as true positive cases.

The study implemented two experiments, as shown in Figure 7, to calculate PSD based on the actual movement velocities of workers and robots and to control the robot's velocity according to the relative distance. FPSD Experiment 1 (Figure 7-(a)) simulated a scenario where the worker and the gantry robot moved simultaneously, causing the relative distance to gradually decrease. FPSD Experiment 2 (Figure 7-(b)) was conducted by setting up a situation in which the worker moved while the collaborative robot performed repetitive tasks, also leading to a reduction in the relative distance.

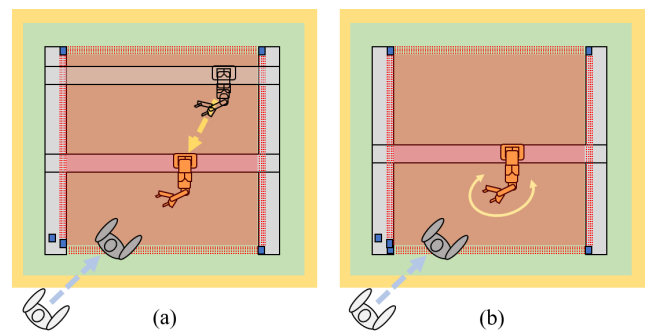


FIGURE 7. Experimental Setup for Flexible Protective Separation Distance (FPSD) Control in Human-Robot Collaboration. (a) FPSD evaluation with simultaneous worker and gantry robot movements, demonstrating adaptive safety control. (b) FPSD evaluation with worker movements during repetitive tasks by a collaborative robot, showcasing dynamic velocity adjustments.

Figure 8 presented the results of FPSD Experiment 1. In this experiment, the FPSD values calculated based on the actual movement velocities of the worker and the gantry robot were used to define the robot's stop distance, while 1.5 times the FPSD value was set as the slow distance. Subsequently, the PSD corresponding to the fixed worker velocities (2.5, 1.6 m/s) proposed in [18], [19], and [20] was compared with the performance of our FPSD.

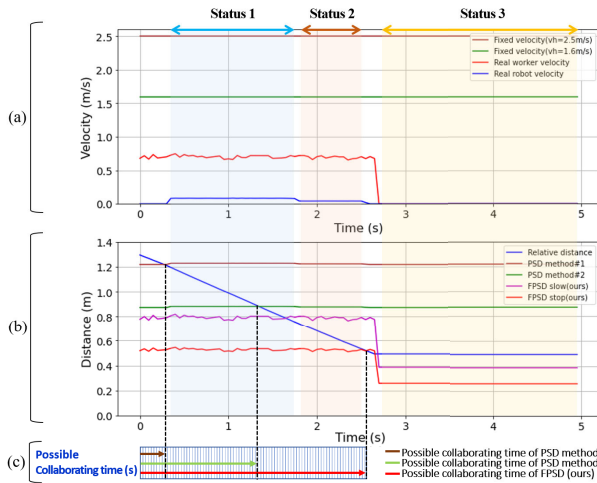


FIGURE 8. Performance Evaluation of Worker-Gantry Robot Collaboration Using Fixed PSD and FPSD. (a) Comparison of fixed and measured velocities of the worker and gantry robot. (b) Relative distance, fixed PSD, and FPSD values over time. (c) Collaboration time (T_c) achieved with FPSD compared to fixed PSD methods, demonstrating enhanced workspace utilization.

Figure 8(a) illustrated the fixed velocities for comparison alongside the measured movement velocities of the worker and the gantry robot in the experiment. Part (b) depicted the relative distance between the worker and the robot measured during the experiment, the PSD values calculated based on the fixed worker velocities, and the FPSD-slow and FPSD-stop calculated using the actual measured velocities of the worker and the robot. Lastly, part (c) visualized the possible collaborating time (T_c) based on the PSDs calculated for the fixed worker velocities and our FPSD.

Table 5 showed the actual velocities of the robot and the worker, the relative distance, and the PSD for the fixed velocities as well as our FPSD for each status depicted in Figure 8. Here, the velocities of the worker and the robot were represented as average values, while the PSD values were presented as range values for each status.

According to the experimental results, the PSD values for the fixed worker velocities were approximately 1.22 m for PSD method#1 and 0.87 m for PSD method#2, showing little variation across all statuses. In contrast, our FPSD showed a slight decrease in distance in Status 2 compared to Status 1, and a significant decrease in Status 3. When the relative distance between the worker and the robot reached the FPSD, the robot's velocity was controlled to

TABLE 5. Comparison of PSD based on the velocities of the worker and the gantry robot.

Data type	Status 1	Status 2	Status 3
Robot velocity	0.0835 m/s	0.0416 m/s	0 m/s
Worker velocity	0.7034 m/s	0.6938 m/s	0 m/s
Relative Distance	1.1959 - 0.7711 m	0.7250 - 0.5204 m	0.4928 m
PSD method#1 [20] ($v_h = 2.5$ m/s)	1.2294 - 1.2289 m	1.2246 - 1.2244 m	1.2199 m
PSD method#2 [20] ($v_h = 1.6$ m/s)	0.8828 - 0.8825 m	0.8781 - 0.8779 m	0.8734 m
FPSD slow (ours)	0.8194 - 0.7697 m	0.8033 - 0.7644 m	0.3861 m
FPSD stop (ours)	0.5463 - 0.5131 m	0.5355 - 0.5096 m	0.2574 m

slow and stop states, effectively preventing collision risks and demonstrating robust control capabilities.

Figure 9 illustrated the results of FPSD Experiment 2. In this experiment, the FPSD values calculated based on the measured velocities of the actual worker and the collaborative robot were compared with the PSD values calculated for the fixed worker velocities.

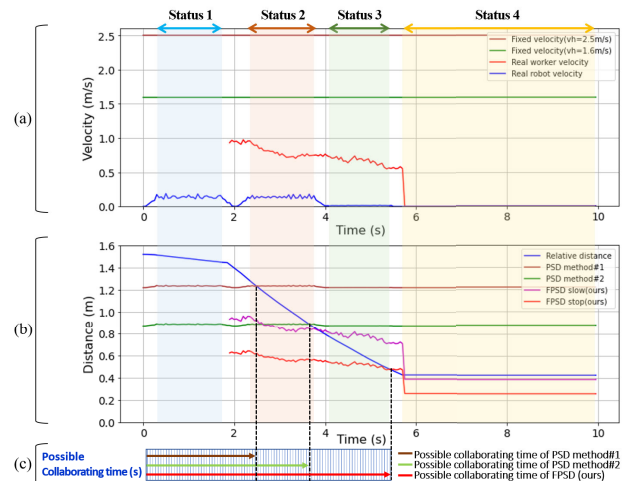


FIGURE 9. Performance Evaluation of Worker-Collaborative Robot Interaction Using Fixed PSD and FPSD. (a) Comparison of fixed and measured velocities of the worker and collaborative robot. (b) Relative distance, fixed PSD, and FPSD values over time. (c) Collaboration time (T_c) achieved with FPSD compared to fixed PSD methods, highlighting improved efficiency and safety.

Figure 9(a) showed the fixed worker velocities as well as the measured velocities of the worker and the collaborative robot from the experiment. Part (b) presented the relative distance between the robot and the worker, the PSD values calculated based on the fixed worker velocities, and the FPSD values calculated based on the actual measured velocities of the worker and the robot. Lastly, Part (c) visualized the possible collaborating time based on the fixed PSD and our FPSD.

Table 6 presented the experimental results shown in Figure 9, including the actual velocities of the robot and the worker measured in each status, the corresponding relative distance, the fixed PSD values, and our FPSD. According to the experimental results, the distances corresponding to PSD method#1 and method#2 for the fixed worker velocities were approximately 1.22 m and 0.87 m, respectively, with minimal variation across all statuses. In contrast, our FPSD, which accounted for the actual worker velocities, demonstrated variations in PSD in States 2, 3, and 4, showing shorter distances compared to PSD method#1 and method#2. These results demonstrate the superiority of our system in flexibly adjusting FPSD based on the velocities of the worker and the robot, and effectively controlling speed as the relative distance decreases.

TABLE 6. Comparison of PSD based on the velocities of the worker and the collaborative robot.

Data type	Status 1	Status 2	Status 3	Status 4
Robot velocity	0.1399 m/s	0.1387 m/s	0.0138 m/s	0 m/s
Worker velocity	None	0.9576 - 0.7431 m/s	0.7277 - 0.5501 m/s	0 m/s
Relative Distance	1.5131 - 1.4451 m	1.2989 - 0.8179 m	0.7684 m 0.4613 m	0.4245 m
PSD method #1 [20] ($v_h = 2.5$ m/s)	1.2409 - 1.2331 m	1.2389 - 1.2323 m	1.2217 - 1.2211 m	1.2199 m
PSD method #2 [20] ($v_h = 1.6$ m/s)	0.8944 - 0.8856 m	0.8934 - 0.8855 m	0.8752 - 0.8744 m	0.8734 m
FPSD slow (ours)	None	0.9618 - 0.8335 m	0.8077 - 0.7153 m	0.3861 m
FPSD stop (ours)	None	0.6412 - 0.5557 m	0.5384 - 0.4769 m	0.2574 m

C. PERFORMANCE ANALYSIS OF FPSD

This study evaluated the performance of the PSD calculated based on fixed worker velocities, as proposed in prior research, against the FPSD reflecting the actual velocities of workers and robots measured during experiments. The results revealed that PSD based on fixed worker velocities showed minimal variation despite robot movement. In contrast, FPSD, by incorporating real-time worker velocities, dynamically adjusted its values as the distance between the worker and robot decreased, effectively reducing robot velocity, mitigating collision risks, and improving work efficiency.

Table 7 summarizes the possible collaborating time (T_c) and utilization rate (R_u) derived from the results in Figures 7(c) and 8(c). In Experiment 1 (Gantry Robot), the

TABLE 7. Comparison of possible collaborating time and utilization rate between PSD for fixed worker velocities and FPSD.

Experiment	Index	Total	PSD method #1 ($v_h = 2.5$ m/s)	PSD method #2 ($v_h = 1.6$ m/s)	FPSD (ours) (Real v_h)
1	T_c (s)	2.55	0.25	1.35	2.50
	R_u (%)	100	9.80	54.94	98.04
2	T_c (s)	5.45	2.50	3.65	5.40
	R_u (%)	100	45.87	66.97	99.08

collaborating times for PSD method#1 and method#2, based on fixed worker velocities, were limited to 0.25 s (9.80%) and 1.35 s (54.94%), respectively. By comparison, FPSD achieved a significantly higher collaborating time of 2.50 s (98.04%) with a near-optimal utilization rate. Similarly, in Experiment 2 (Collaborative Robot), PSD method#1 and method#2 yielded collaborating times of 2.50 s (45.87%) and 3.65 s (66.97%), respectively, while FPSD recorded the longest collaborating time of 5.40 s (99.08%) and the highest utilization rate.

In conclusion, PSD based on fixed worker speed cannot adapt to real-time worker movements, which limits collaboration time and reduces utilization. In contrast, FPSD significantly increases collaboration time and maximizes workspace utilization by dynamically adjusting the robot's response based on proximity. These improvements have meaningful implications for real-world collaborative robot environments. For example, in Experiment 1, FPSD effectively triples the available interaction window with the gantry robot by increasing the collaboration time by 2.25 s compared to PSD method#1 and by 1.15 s compared to Method#2. In Experiment 2, FPSD's collaboration time is 5.40 s (compared to 2.50 s and 3.65 s for PSD method), more than doubling the collaboration period with the robot. This extended interaction period reduces unnecessary pauses, allowing the worker and robot to maintain workflow continuity, which directly translates into higher throughput and operational efficiency in tasks such as assembly or material handling. Therefore, we confirm that FPSD can effectively improve task efficiency in collaborative robot environments in human-robot collaborative environments.

V. CONCLUSION

The proposed AI-based Digital Twin technique enhances collaborative robotics by overcoming the limitations of conventional sensor-based safety systems, enabling adaptive and efficient human-robot collaboration. By integrating real-time multi-domain vision sensor data, the method accurately estimates the worker's 3D skeletal positions and dynamically calculates a FPSD, surpassing the static constraints of ISO/TS 15066 standards. Experimental results demonstrate that FPSD significantly outperforms fixed PSD approaches, achieving collaboration times of 2.50 s (98.04%) compared to 0.25 s (9.80%) and 1.35 s (54.94%) in Experiment 1 (Gantry Robot), and 5.40 s (99.08%) versus 2.50 s (45.87%) and 3.65 s (66.97%) in Experiment 2 (Collaborative Robot). These extended interaction periods minimize unnecessary pauses, improving workflow continuity and operational efficiency in tasks such as assembly and material handling.

This flexible safety control framework is well-suited for smart manufacturing environments, including assembly lines and dynamic material transport systems, ensuring both safety and productivity through real-time adaptation to worker and robot velocities. However, the study evaluated gantry and collaborative robots independently, limiting insights into multi-robot coordination. Future research will

validate FPSD in simultaneous multi-robot operations and complex worker-robot interaction scenarios, focusing on practical challenges such as multi-robot synchronization, sensor interference, and integration with existing manufacturing execution systems. To further improve the system's robustness and applicability in real-world deployments, future work will also expand the scope of experimental conditions and introduce formal evaluation metrics—such as true/false positive and negative rates—to enable more rigorous performance assessment. Additionally, developing adaptive speed adjustment and emergency stop strategies based on behavior-specific risk levels will involve testing with heterogeneous robot fleets (e.g., combining articulated and mobile robots) to ensure compatibility and safety in dynamic environments. These efforts will be supported by small-scale simulations to optimize sensor placement and mitigate issues like occlusion or latency in high-density workspaces.

In the current study, parameters C , Z_d , and Z_r were set to zero due to sufficient surveillance coverage, a small workspace, constant robot speed, and slow worker approach in the simulation. In real industrial settings, however, factors like limited camera coverage, sensor measurement errors, and system precision introduce complexities. Future work will incorporate C , Z_d , and Z_r to calculate more accurate and reliable FPSD values, using field data from operational factories to account for environmental noise, variable lighting, and worker fatigue. Practical calibration methods for these parameters will be developed to facilitate deployment in small- and medium-sized enterprises with constrained resources, ensuring cost-effective implementation.

ACKNOWLEDGMENT

(Ji Dong Choi and Seung-Hwan Choi are co-first authors.)

REFERENCES

- [1] *Robots and Robotic Devices—Collaborative Robots*, ISO Standard 15066:2016, 2016. [Online]. Available: <https://www.iso.org/standard/62996.html>
- [2] A. Ghanbarzadeh and E. Najafi, "Safe physical human–robot interaction through variable impedance control based on ISO/TS 15066," 2023, *arXiv:2311.13814*.
- [3] A. Golshani, A. Kouhord, A. Ghanbarzadeh, and E. Najafi, "Control design for safe human–robot collaboration based on ISO/TS 15066 with power and force limit," in *Proc. 11th RSI Int. Conf. Robot. Mechatronics (ICRoM)*, Dec. 2023, pp. 279–284.
- [4] Y. Kang, D. Kim, and D. Yun, "Manipulator collision avoidance system based on a 3D potential field with ISO 15066," *IEEE Access*, vol. 10, pp. 126593–126602, 2022.
- [5] Y. E. Cogurcu, J. A. Douthwaite, and S. Maddock, "A comparative study of safety zone visualisations for virtual and physical robot arms using augmented reality," *Computers*, vol. 12, no. 4, p. 75, Apr. 2023.
- [6] P. Long, C. Chevallereau, D. Chablat, and A. Girin, "An industrial security system for human–robot coexistence," *Ind. Robot, Int. J.*, vol. 45, no. 2, pp. 220–226, Apr. 2018.
- [7] J. Park, L. Carøe Sørensen, S. Faarvang Mathiesen, and C. Schlette, "A digital twin-based workspace monitoring system for safe human–robot collaboration," in *Proc. 10th Int. Conf. Control, Mechatronics Autom. (ICCA)*, Nov. 2022, pp. 24–30.
- [8] *Robots and Robotic Devices Safety Requirements for Industrial Robots Part 1: Robots*, ISO Standard 10218-1:2011, 2011. [Online]. Available: <https://www.iso.org/standard/51330.html>
- [9] *Robots and Robotic Devices Safety Requirements for Industrial Robots Part 2: Robot Systems and Integration*, ISO Standard 10218-2:2011, 2011. [Online]. Available: <https://www.iso.org/standard/41571.html>
- [10] P. Chemweno, L. Pintelon, and W. Decre, "Orienting safety assurance with outcomes of hazard analysis and risk assessment: A review of the ISO 15066 standard for collaborative robot systems," *Saf. Sci.*, vol. 129, Sep. 2020, Art. no. 104832.
- [11] *Safety of Machinery Positioning of Safeguards With Respect to the Approach Speeds of Parts of the Human Body*, ISO Standard 13855:2010, 2010. [Online]. Available: <https://www.iso.org/standard/42845.html>
- [12] V. Villani, F. Pini, F. Leali, and C. Secchi, "Survey on human–robot collaboration in industrial settings: Safety, intuitive interfaces and applications," *Mechatronics*, vol. 55, pp. 248–266, Nov. 2018.
- [13] S. Haddadin, A. De Luca, and A. Albu-Schäffer, "Robot collisions: A survey on detection, isolation, and identification," *IEEE Trans. Robot.*, vol. 33, no. 6, pp. 1292–1312, Dec. 2017.
- [14] P. A. Lasota, G. F. Rossano, and J. A. Shah, "Toward safe close-proximity human–robot interaction with standard industrial robots," in *Proc. IEEE Int. Conf. Autom. Sci. Eng. (CASE)*, Aug. 2014, pp. 339–344.
- [15] S. Robla-Gómez, V. M. Becerra, J. R. Llata, E. González-Sarabia, C. Torre-Ferrero, and J. Pérez-Oria, "Working together: A review on safe human–robot collaboration in industrial environments," *IEEE Access*, vol. 5, pp. 26754–26773, 2017.
- [16] Y. Cheng, W. Zhang, and K. Hauser, "Learning to avoid unsafe actions in reinforcement learning for cooperative human–robot tasks," in *Proc. IEEE Int. Conf. Robot. Autom. (ICRA)*, May 2019, pp. 2386–2392.
- [17] C. Liu, J. Hu, and Y. Wang, "Human motion prediction for human–robot collaboration: A deep learning approach," *IEEE Access*, vol. 8, pp. 102675–102687, 2020.
- [18] U. B. Himmelsbach, T. M. Wendt, N. Hangst, P. Gawron, and L. Stiglmeier, "Human–machine differentiation in speed and separation monitoring for improved efficiency in human–robot collaboration," *Sensors*, vol. 21, no. 21, p. 7144, Oct. 2021.
- [19] P. Karagiannis, N. Kousi, G. Michalos, K. Dimoulas, K. Mparis, D. Dimosthenopoulos, Ö. Tokalar, T. Guasch, G. Gerio, and S. Makris, "Adaptive speed and separation monitoring based on switching of safety zones for effective human robot collaboration," *Robot. Comput.-Integr. Manuf.*, vol. 77, Oct. 2022, Art. no. 102361.
- [20] D. Podgorelec, S. Uran, A. Nerat, B. Bratina, S. Pečnik, M. Dimec, F. Žaberl, B. Žalik, and R. Šafarič, "LiDAR-based maintenance of a safe distance between a human and a robot arm," *Sensors*, vol. 23, no. 9, p. 4305, Apr. 2023.
- [21] G. Yang, H. Zhang, L. Wang, J. Li, R. Wang, and D. Kong, "A digital twin based large-area robot skin system for safer human-centered healthcare robots toward Healthcare 4.0," *IEEE Trans. Med. Robot. Bionics*, vol. 6, no. 2, pp. 142–155, Feb. 2024.
- [22] Z. V. Gbouna, G. Pang, G. Yang, Z. Hou, H. Lv, Z. Yu, and Z. Pang, "User-interactive robot skin with large-area scalability for safer and natural human–robot collaboration in future telehealthcare," *IEEE J. Biomed. Health Informat.*, vol. 25, no. 12, pp. 4276–4288, Dec. 2021.
- [23] R. Wang, C. Li, H. Lyu, G. Pang, H. Wu, and G. Yang, "A smooth velocity transition framework based on hierarchical proximity sensing for safe human–robot interaction," *IEEE Robot. Autom. Lett.*, vol. 9, no. 6, pp. 4910–4917, Jun. 2024.
- [24] G. Pang, G. Yang, and Z. Pang, "Review of robot skin: A potential enabler for safe collaboration, immersive teleoperation, and affective interaction of future collaborative robots," *IEEE Trans. Med. Robot. Bionics*, vol. 3, no. 3, pp. 681–700, Aug. 2021.
- [25] Z. Cao, G. Hidalgo, T. Simon, S.-E. Wei, and Y. Sheikh, "OpenPose: Realtime multi-person 2D pose estimation using part affinity fields," 2018, *arXiv:1812.08008*.
- [26] N. Gelfand, L. Ikemoto, S. Rusinkiewicz, and M. Levoy, "Geometrically stable sampling for the ICP algorithm," in *Proc. 4th Int. Conf. 3-D Digit. Imag. Modeling*, Oct. 2003, pp. 260–267.
- [27] G. C. Amaizu, J. N. Njoku, J.-M. Lee, and D.-S. Kim, "Metaverse in advanced manufacturing: Background, applications, limitations, open issues & future directions," *ICT Exp.*, vol. 10, no. 2, pp. 233–255, Apr. 2024.
- [28] K. T. Park, Y. W. Nam, H. S. Lee, S. J. Im, S. D. Noh, J. Y. Son, and H. Kim, "Design and implementation of a digital twin application for a connected micro smart factory," *Int. J. Comput. Integr. Manuf.*, vol. 32, no. 6, pp. 596–614, Jun. 2019.

- [29] E. Glaessgen and D. Stargel, "The digital twin paradigm for future NASA and U.S. air force vehicles," in *Proc. 53rd AIAA/ASME/ASCE/AHS/ASC Struct., Struct. Dyn. Mater. Conf. 20th AIAA/ASME/AHS Adapt. Struct. Conf.*, Apr. 2012, p. 1818.
- [30] Y. Chen, "Integrated and intelligent manufacturing: Perspectives and enablers," *Engineering*, vol. 3, no. 5, pp. 588–595, Oct. 2017.
- [31] Z. Liu, N. Meyendorf, and N. Mrad, "The role of data fusion in predictive maintenance using digital twin," in *Proc. AIP Conf.*, Provo, UT, USA, 2018, p. 20023.
- [32] A. Fuller, Z. Fan, C. Day, and C. Barlow, "Digital twin: Enabling technologies, challenges and open research," *IEEE Access*, vol. 8, pp. 108952–108971, 2020, doi: [10.1109/ACCESS.2020.2998358](https://doi.org/10.1109/ACCESS.2020.2998358).
- [33] A. Chatzitofis, D. Zarpalas, S. Kollias, and P. Daras, "DeepMoCap: Deep optical motion capture using multiple depth sensors and retro-reflectors," *Sensors*, vol. 19, no. 2, p. 282, Jan. 2019.



JI DONG CHOI received the M.S. degree from Kyungpook National University (KNU), Daegu, South Korea, in 2022, where he is currently pursuing the Ph.D. degree. He is a member of the Mobility Systems Group, Korea Institute of Industrial Technology (KITECH). His research interests include signal processing using multi-domain sensor data, pose estimation, camera pose estimation, and robot pose estimation.



SEUNG-HWAN CHOI received the M.S. degree in robotics convergence from Pusan National University, Busan, South Korea, in 2014, where he is currently pursuing the Ph.D. degree. He is a member of the Advanced Mobility System Group, Korea Institute of Industrial Technology (KITECH). His research interests include sensor data-based signal processing and the application of AI algorithms for anomaly detection in mechanical devices and robots.



MIN YOUNG KIM (Member, IEEE) received the B.S., M.S., and Ph.D. degrees from Korea Advanced Institute of Science and Technology, South Korea, in 1996, 1998, and 2004, respectively. From 2004 to 2005, he was a Senior Researcher with Mirae Corporation. From 2005 to 2009, he was a Chief Research Engineer with Kohyoung Corporation in the research field of artificial vision systems for intelligent machines and robots. Since 2009, he has been an Assistant

Professor with the School of Electrical Engineering and Computer Science, Kyungpook National University. From 2014 to 2016, he was a Visiting Associate Professor with the Department of Electrical and Computer Engineering, School of Medicine, Johns Hopkins University. He is currently an Associate Professor with the School of Electronics Engineering, Kyungpook National University. He is also the Deputy Director of the KNULG Convergence Research Center and the Director of the Research Center for Neurosurgical Robotic Systems. His research interests include the visual intelligence for robotic perception and recognition of autonomous ground and aerial vehicles.



INHO LEE (Member, IEEE) received the B.S., M.S., and Ph.D. degrees in mechanical engineering from Korea Advanced Institute of Science and Technology (KAIST), Daejeon, South Korea, in 2009, 2011, and 2016, respectively. He was working on the project of development for humanoid robots: HUBO, HUBO2, and DRC-HUBO. In 2015, he was a Team Member of TEAM KAIST which is the winning team for the DARPA Robotics Challenge. He was with the Institute for Human and Machine Cognition Robotics Laboratory (IHMC). He is currently with Pusan National University. His research interests include motion planning, quadruped and bipedal walking, and stabilization control for a humanoid robot, quadrotors, manipulation, sensors, actuators, and application of microprocessors.



SUWOONG LEE received the M.S. and Ph.D. degrees in engineering from the University of Tsukuba, Japan, in 2002 and 2005, respectively. He was a Postdoctoral Fellow with the Safety Intelligence Research Group, Intelligent Systems Research Institute, National Institute of Advanced Industrial Science and Technology, Japan, from 2005 to 2009, and an Assistant Professor with the Department of Bio-Systems Engineering, Graduate School of Science and Engineering, Yamagata University, Japan, from 2009 to 2012. He is currently a Principal Researcher with the Advanced Mobility System Group, Korea Institute of Industrial Technology (KITECH). His research interests include sensor-fusion, human-cooperative robot, human-machine interface, and robot safety.



BYEONG HAK KIM received the Ph.D. degree from the School of Electronic Engineering, Kyungpook National University (KNU), Daegu, South Korea. He was a Senior Engineer with the Department of Optronics, Samsung Thales, and Hanwha System Company, South Korea. From 2018 to 2019, he was a Visiting Collaborative Researcher with the Faculty of Computer Science, Ljubljana University, Ljubljana, Slovenia. Since 2020, he has been a Senior Researcher with Korea Institute of Industrial Technology (KITECH). His current research interests include AI + digital twin, LiDAR sensor development, TIR image enhancement, visual object tracking, foundation AI model for 3D object detection and segmentation, laser radar, and remote sensing systems.

...